

<https://doi.org/10.1038/s43247-025-02708-0>

Divergent impacts of climate interventions on China's north-south water divide



Xiao Zhang¹, Yuanchao Fan¹✉, Jerry Tjiputra², Helene Muri^{3,4} & Qiao Chen⁵

Solar radiation modification-based climate interventions may cause uneven regional hydrological changes while mitigating warming. Here, we investigate the effects of climate interventions on China's North Drought-South Flood pattern using the Norwegian Earth System Model supplemented by volcanic data. Our results indicate that equatorial stratospheric aerosol injection could mitigate the north-south water divide by reducing inter-hemispheric and equator-to-North-pole temperature gradients, thereby modifying atmospheric circulation and the East Asian monsoon to increase precipitation and surface runoff in northern China while reducing them in the south, compared to the high emissions scenario. This mechanism is supported by observed precipitation changes following the Mount Pinatubo volcanic eruption. In contrast, marine cloud brightening may intensify southern flood risks, while cirrus cloud thinning and moderate emissions reduction might exacerbate northern droughts. Our findings reveal distinct regional hydroclimatic impacts of different climate interventions, highlighting potential synergies and trade-offs between their global intervention efficacy and regional water security.

The global surface air temperature is accelerating faster than expected and without radical emission reductions, the Earth is on track to breach the 1.5 °C warming threshold of the Paris climate target¹. Mitigating global warming remains challenging due to difficulties and costs in reducing emissions², prompting the exploration of solar or longwave radiation modification-based climate intervention strategies (SRM for short, and many other terms exist)³. The Geoengineering Model Inter-comparison Project⁴ has proposed three SRM climate interventions: Stratospheric Aerosol Injection (SAI), Marine Cloud Brightening (MCB), and Cirrus Cloud Thinning (CCT), which involves modifying the reflectivity of the atmosphere (SAI, MCB) or altering longwave radiation emissivity (CCT) to reduce net radiative forcing at the Earth's surface. Existing studies have revealed that different SRM schemes can achieve similar global temperature targets but produce distinct regional climate and hydrological patterns⁵. The regionally unequal effects of SRM on climate⁶ and hydrological cycles⁷ and large uncertainties of the Earth system response to SRM have stimulated continuous debates⁸. It is therefore essential to conduct comprehensive and systematic assessments of the impacts of SRM across different Earth system components before any implementation of such large-scale intervention measures.

Research on SAI has mainly shown that reducing surface shortwave radiation and average temperature may lower global mean precipitation⁹ and decrease the frequency of extreme events like heatwaves and heavy rainfall worldwide^{10,11}. Studies on MCB reveal minimal changes in global mean precipitation but substantial regional variations depending on the design and simulation method^{5,12}. For CCT, most studies suggest it could enhance the global water cycle by increasing longwave radiation emission and surface solar shortwave radiation^{5,13}, though some studies report negligible¹⁴ or reduced¹⁵ global precipitation changes. The notable differences in the effects of SAI, MCB, and CCT highlight the complexity and uncertainty of hydrological responses to varying SRM methods and deployment strategies.

While prior studies have examined the hydrological effects of individual SRM methods, predominantly SAI, on global and regional precipitation patterns^{16–20}, comprehensive evaluations of multiple SRM methods within a consistent modeling framework remain scarce. This gap is particularly evident in studies of regional hydroclimate impacts in East Asia, where complex monsoon dynamics and pronounced spatial heterogeneity in water resources^{21–23} present unique challenges for climate intervention assessment.

¹Institute of Environment and Ecology, Tsinghua Shenzhen International Graduate School, Tsinghua University, Shenzhen, China. ²NORCE Research AS, Bjerknes Centre for Climate Research, Bergen, Norway. ³Industrial Ecology Programme, Department of Energy and Process Engineering, Norwegian University of Science and Technology, Trondheim, Norway. ⁴NILU, Kjeller, Norway. ⁵Three Gorges Research Center for Ecology and Environment, Chongqing Institute of Green and Intelligent Technology, Chinese Academy of Sciences, Chongqing, China. ✉e-mail: yuanchao.fan@sz.tsinghua.edu.cn

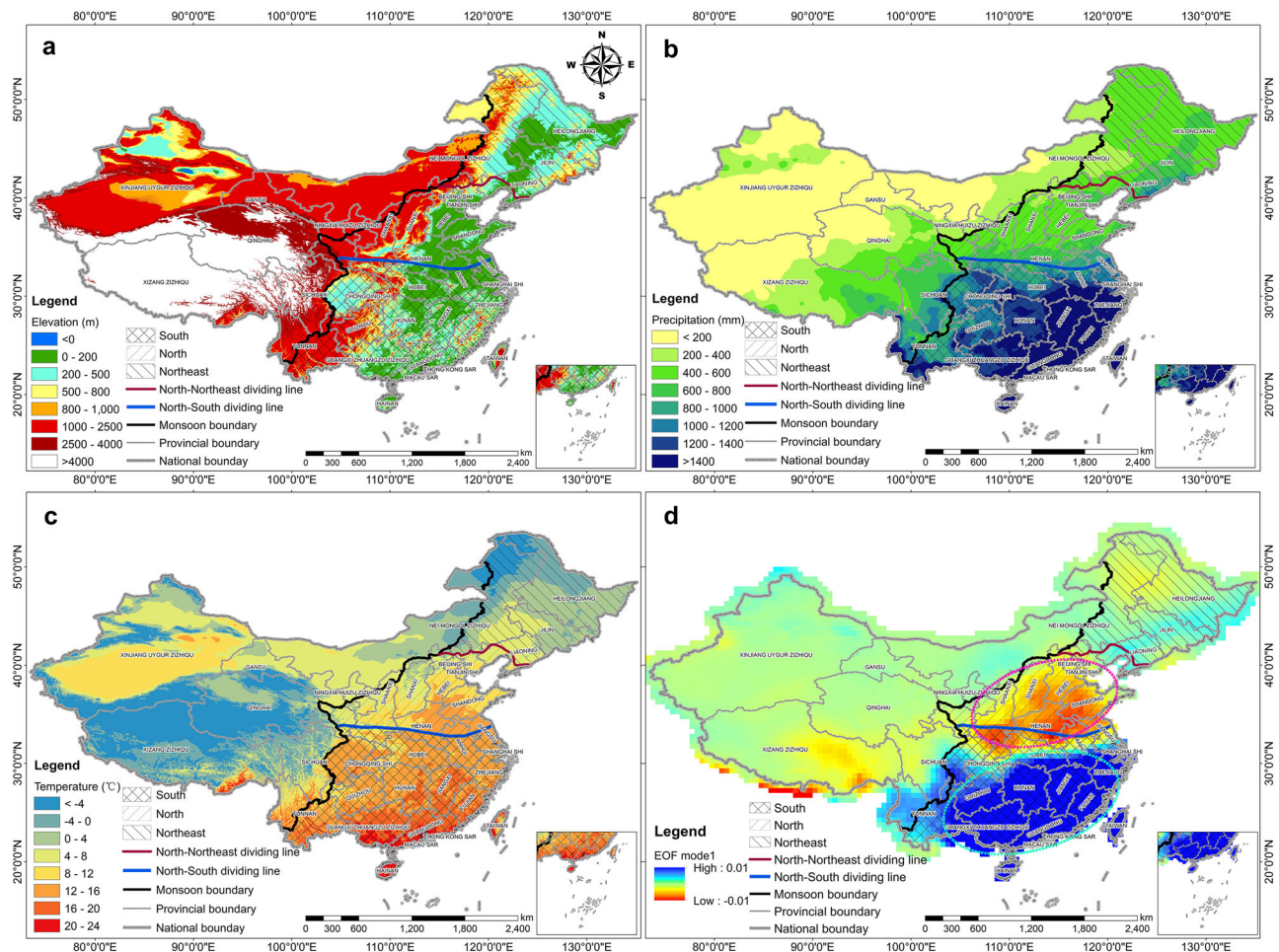


Fig. 1 | The monsoon region and its north-south division in China. a Topography and climate zones; **b** Precipitation climatology; **c** Temperature climatology; **d** The first Empirical Orthogonal Function (EOF) mode of precipitation (1901–2020) over China. Topography data is from the Copernicus Global Digital Elevation Model⁹⁶. Precipitation climatology and temperature climatology is based on observations from 1960 to 2021 in China⁹⁷. The EOF in **d** was calculated based on data from the Climate Research Unit (CRU ts4.06). The monsoon region encompasses major river basins in Eastern China (east of the black line), based on GIS Dataset of Boundaries among four Geo-Eco Regions of China⁹⁸. The Qinling mountain range-Huaihe river (blue line, around 33°N) in the monsoon region is typically regarded as the dividing

line between northern and southern China, with the south being wetter and the north being drier in terms of annual precipitation (**b**)⁹⁹. The climatic boundary (red line, around 41°N) between the warm temperate zone and the mid-temperate zone (**c**)¹⁰⁰ further divides the monsoon region to northern and northeastern regions. The dashed ellipses in **d** characterize the well-known North-Drought (pink ellipse) South-Flood (cyan ellipse) hydrological division (NDSF) of China^{60,101,102}. This study focuses on the relatively drier northern monsoon (between red and blue lines) and wetter southern monsoon (south of blue line) regions, largely consistent with NDSF regions, to analyze climate intervention impacts on NDSF.

East Asia's hydroclimate is characterized by the persistent North Drought-South Flood (NDSF) pattern, which creates an uneven distribution of water resources with abundance in southern China and scarcity in the north²⁴ (see Fig. 1 for the monsoon region and its north-south division). This pattern has prevailed during most warm periods over the past 2000 years^{25,26}, contributing to recurring extreme drought and flood events^{27,28}. Continued global warming threatens to intensify these disparities through accelerated snow cover loss and glacier retreat on the Tibetan Plateau²⁹, as well as strengthened East Asian monsoon variability³⁰. Understanding how different SRM approaches might alter these established hydroclimate patterns is, therefore, critical for assessing both the potential benefits and risks of climate interventions in one of the world's most populous regions.

To our knowledge, no previous study has systematically compared the effects of the three major SRM strategies (SAI, MCB, and CCT), on the NDSF pattern. Given the potential for each method to influence atmospheric circulation, monsoon dynamics, and surface water availability in different ways^{3,31}, it is a critical research gap that needs to be filled. Our study addresses this gap by employing the Norwegian Earth System Model (NorESM1-ME)³² to evaluate and contrast the regional hydroclimatic

impacts of SAI, MCB, and CCT on the NDSF under a high-emissions scenario. The three SRM schemes were designed to achieve similar net radiative forcing to that of a moderate emissions reduction scenario (RCP4.5) relative to RCP8.5 (see Methods). The three SRMs and RCP4.5 are all compared to RCP8.5 in the same period (2070–2099) to quantify their effects on the monsoon system and surface runoff. By isolating the distinct dynamical and thermodynamic responses associated with each method, we aim to provide the first comparative assessment of how these climate interventions might mitigate or exacerbate China's longstanding north-south water divide.

Results

Surface runoff responses to climate interventions or mitigation

In the absence of climate intervention or mitigation, the NorESM1-ME projects increased precipitation and runoff under RCP8.5 (Supplementary Fig. 1), especially in the south of China's monsoon region (Supplementary Fig. 2), which would exacerbate the NDSF—a finding that aligns with multi-model mean projections using data from the Coupled Model Inter-comparison Project phase 6 (CMIP6; Supplementary Fig. 3) and the

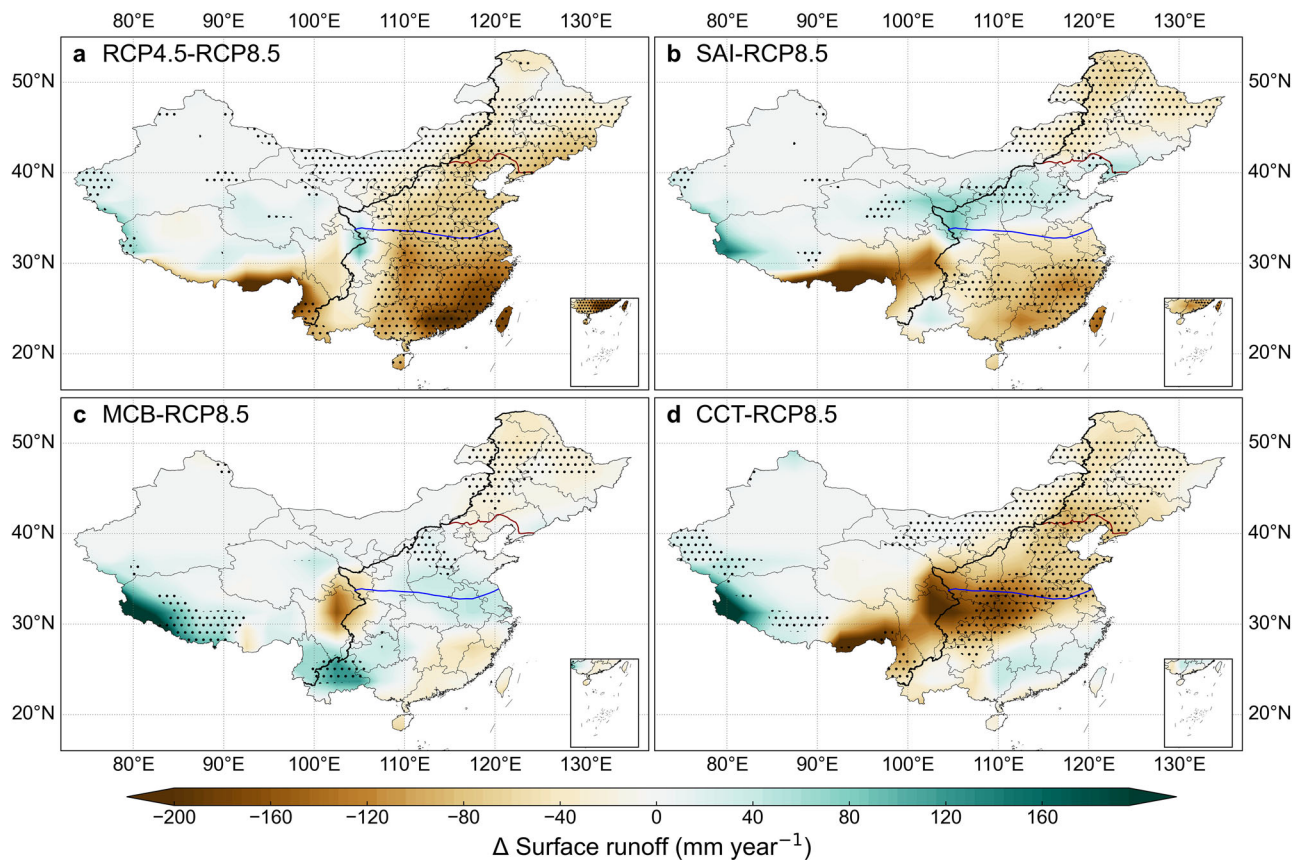


Fig. 2 | Projected differences in annual surface runoff in China under emissions reduction and climate interventions relative to RCP8.5. a RCP4.5 minus RCP8.5; b SAI minus RCP8.5; c MCB minus RCP8.5; d CCT minus RCP8.5 in the period 2070–2099. Dots indicate differences that are statistically significant at the 95% confidence level ($p < 0.05$). The black line denotes the monsoon boundary, the area

between red and blue lines denotes the northern monsoon region and the south of blue line denotes the southern monsoon region (see more details in Fig. 1). Each panel includes an inset map showing the South China Sea region to ensure cartographic completeness of China's territorial boundaries. These insets maintain standard mapping conventions while preserving the main Fig.'s focus on large-scale patterns.

literature³³. The projected runoff differences (Fig. 2) under climate intervention (SRMs) or mitigation (RCP4.5) relative to RCP8.5 suggest that SAI is the only scenario that could potentially mitigate the NDSF pattern by increasing surface runoff in the north and decreasing it in the south (Fig. 2b). Our attribution analysis (Supplementary Note 1) shows that runoff changes under SRMs are predominantly driven by changes in precipitation and evapotranspiration (ET) or potential evapotranspiration (PET) (more details in Supplementary Note 2 and Supplementary Tables 2–4). Under SAI, precipitation is projected to decrease substantially in the south but slightly increase in the North China Plain (Supplementary Fig. 4b), while ET is projected to uniformly decrease across the north and south (Supplementary Fig. 5b). These changes together result in a net surface runoff increase in the north ($+21.3 \text{ mm year}^{-1}$) and a decrease in the south ($-63.5 \text{ mm year}^{-1}$) of the monsoon region (Table 1). In contrast, MCB and CCT are projected to exacerbate the NDSF by increasing surface runoff in the south and decreasing it in the north (Fig. 2c, d; Table 1), respectively, compared to RCP8.5. The difference between MCB and CCT lies in their drivers (Table 1; Supplementary Figs. 6–8): MCB-induced runoff changes stem from reduced PET due to cooling, while CCT-induced runoff changes are dominated by precipitation reduction. Under RCP4.5, increased ET (Supplementary Fig. 5a) due to enhanced stomatal conductance under lower CO_2 levels relative to RCP8.5 leads to dominant negative land surface effects (soil and vegetation feedbacks), surpassing climate effects (precipitation and PET changes). Their combined effects would alleviate southern floods but exacerbate northern aridity (Fig. 2a and Table 1).

Considering the intra-annual runoff changes in China's monsoon region, SAI would effectively alleviate NDSF by increasing runoff from summer to winter, especially during the crop-growing season

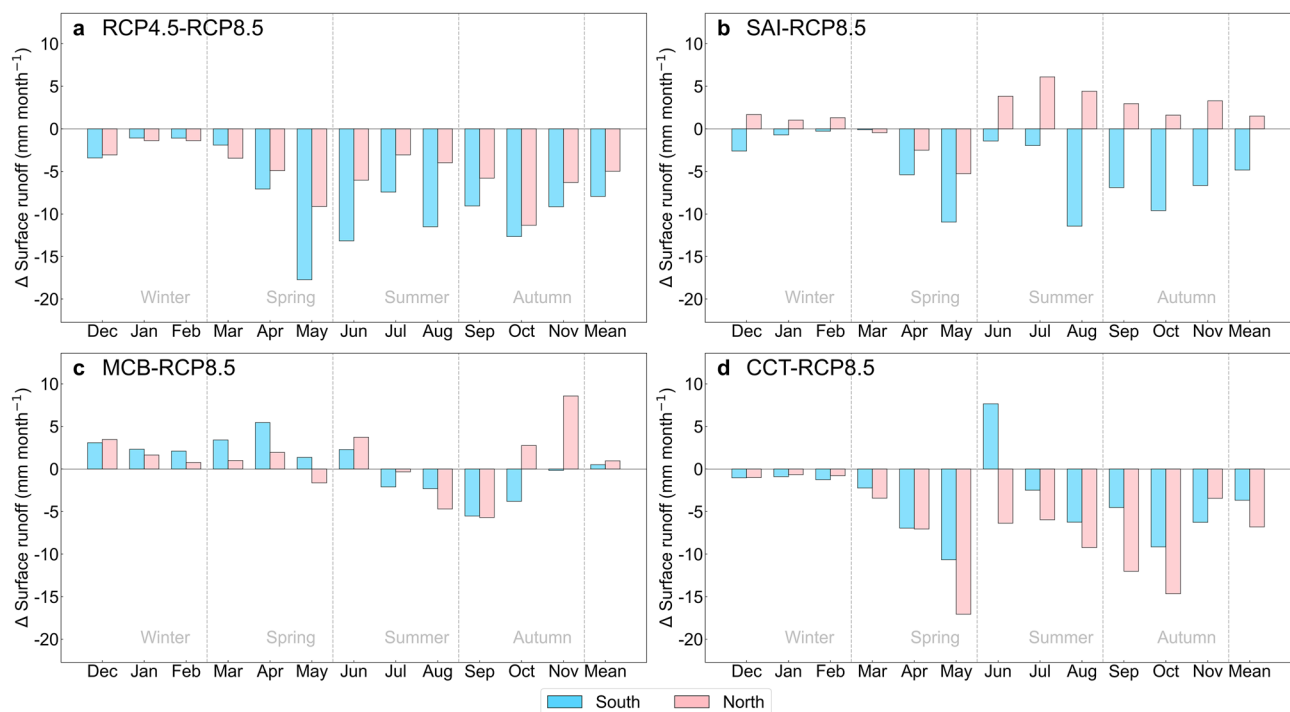
(June–September) in the north, while decreasing it throughout the year, especially during the flood season (April–October) in the south (Fig. 3b). This is primarily achieved by altering the NDSF pattern of summer monsoon precipitation (Supplementary Fig. 6b) and ET changes (Supplementary Fig. 7b) compared to RCP8.5 (more in the next section). Under other scenarios, surface runoff is projected to decline on average during the main flood season (July–September) across the monsoon region. MCB (Fig. 3c) would dramatically increase the risk of floods in early-flood season (April–June). CCT (Fig. 3d) would briefly increase surface runoff in the south in June but cause sustained runoff reduction across monsoon regions throughout the rest of the year, potentially exacerbating drought risks compared to RCP8.5. RCP4.5 is also projected to notably reduce flood risks in the south but increase drought risks in the north by reducing northern surface runoff (Fig. 3a) and precipitation (Supplementary Figs. 4a and 6a) for nearly the entire year.

Analysis of extreme runoff events shows that SAI would also substantially reduce the frequencies of P5 (recurrence interval of 20 years) and P10 (recurrence interval of 10 years) flood events in the flood-prone southern China with relatively small changes in the north (Fig. 4c, e), but slightly increase the duration of P5 and P10 events in south and north of the monsoon regions (Fig. 4d, f). This is consistent with reduced extreme precipitation events compared to warming scenarios found in other SAI studies, particularly in southern China³⁴. Slight increases in P10 events are projected in the North China Plain (Supplementary Fig. 10c). The heterogeneous north-south changes in extreme runoff events counterbalance the NDSF pattern by reducing flood risks overall, which would otherwise increase under RCP8.5 (Supplementary Fig. 9 and ref. 35). The duration of extreme runoff events shows no notable north-south differences and is

Table 1 | Attribution analysis of surface runoff change under RCP8.5 (2070–2099 minus 2006–2035) and under SRMs or emissions reduction (RCP4.5) scenarios compared to RCP8.5 during 2070–2099

| Region | Attribution [mm year ⁻¹ (%)] | RCP8.5 | RCP4.5-RCP8.5 | SAI-RCP8.5 | MCB-RCP8.5 | CCT-RCP8.5 |
|---------------|---|-----------------|-----------------|----------------|---------------|----------------|
| China | P_rf | 98.2 (34.6%) | −32.8 (−9.4%) | −46.7 (−13.4%) | −9.5 (−2.7%) | −33.5 (−9.6%) |
| | PET_rf | −77.0 (−27.1%) | 34.0 (9.8%) | 31 (8.9%) | 23.9 (6.9%) | 9.1 (2.6%) |
| | CC_rf | 21.2 (7.5%) | 1.2 (0.4%) | −15.7 (−4.5%) | 14.3 (4.1%) | −24.5 (−7%) |
| | LS_rf | 63.3 (22.3%) | −45.8 (−13.1%) | −12.4 (−3.6%) | −7.3 (−2.1%) | −5.7 (−1.6%) |
| | Net change | 84.5 (29.8%) | −44.5 (−12.8%) | −28.1 (−8.1%) | 7.0 (2.0%) | −30.1 (−8.6%) |
| North-monsoon | P_rf | 99.7 (24.6%) | −39.7 (−8.5%) | −15.9 (−3.4%) | −14 (−3%) | −73.6 (−15.8%) |
| | PET_rf | −107.5 (−26.5%) | 47.5 (10.2%) | 42.5 (9.1%) | 21.6 (4.6%) | −0.2 (0%) |
| | CC_rf | −7.9 (−1.9%) | 7.9 (1.7%) | 26.7 (5.7%) | 7.6 (1.6%) | −73.8 (−15.9%) |
| | LS_rf | 68.1 (16.8%) | −59.1 (−12.7%) | −5.4 (−1.2%) | −1.3 (−0.3%) | −10.7 (−2.3%) |
| | Net change | 60.3 (14.9%) | −51.2 (−11%) | 21.3 (4.6%) | 6.3 (1.3%) | −84.5 (−18.2%) |
| South-monsoon | P_rf | 144.6 (31%) | −54.8 (−8.8%) | −79.1 (−12.7%) | −23.1 (−3.7%) | −39.9 (−6.4%) |
| | PET_rf | −130.6 (−28%) | 56.3 (9%) | 41.6 (6.7%) | 38.3 (6.2%) | 3.7 (0.6%) |
| | CC_rf | 14.0 (3.0%) | 1.5 (0.2%) | −37.6 (−6%) | 15.2 (2.4%) | −36.2 (−5.8%) |
| | LS_rf | 142.5 (30.6%) | −100.9 (−16.2%) | −25.9 (−4.2%) | −12.7 (−2%) | −8.7 (−1.4%) |
| | Net change | 156.5 (33.6%) | −99.4 (−16%) | −63.5 (−10.2%) | 2.5 (0.4%) | −45 (−7.2%) |

P_rf and PET_rf represent the individual contributions of precipitation and potential evapotranspiration (PET) changes to surface runoff changes, respectively; CC_rf represents the total contribution of climate change to surface runoff changes ($CC_rf = P_rf + PET_rf$); LS_rf represents the contribution of land surface effects to surface runoff changes. South refers to the southern monsoon area, north refers to the northern monsoon area as shown in Fig. 1. Values in parentheses indicate percentage change of surface runoff relative to RCP8.5. The RCP8.5 column shows the relative change rates in the future period (2070–2099) under the RCP8.5 scenario compared to the historical period (2006–2035). The other four columns represent relative change rates in the future period (2070–2099) under SRMs or RCP4.5 scenarios compared to the RCP8.5 scenario.

**Fig. 3 | The intra-annual distribution of differences in surface runoff under emissions reduction and climate interventions relative to RCP8.5. a RCP4.5 minus RCP8.5; b SAI minus RCP8.5; c MCB minus RCP8.5; d CCT minus RCP8.5 in**

the period 2070–2099. Cyan and pink bars indicate surface runoff differences in the southern and northern parts of the monsoon region in China, respectively (see the north-south and monsoon boundaries in Fig. 1).

projected to decrease for P1 (recurrence interval of 100 years) and increase for P5 and P10 events compared to RCP8.5.

MCB is projected to reduce the frequency (Fig. 4e, Supplementary Fig. 10e) but increase the duration (Fig. 4f, Supplementary Fig. 10f) of P10 events in the south monsoon region, whereas CCT is projected to reduce the

frequencies of P10 (Fig. 4e, Supplementary Fig. 10g) and P5 (Fig. 4c, Supplementary Fig. 11g) events in most monsoon regions. RCP4.5 is projected to reduce the frequency of P10 events and the durations of P10 and P5 events across most monsoon regions (Fig. 4; Supplementary Figs. 10a, b, and 11b). For more extreme runoff events (P1, Fig. 4a, b, Supplementary Fig. 12), most

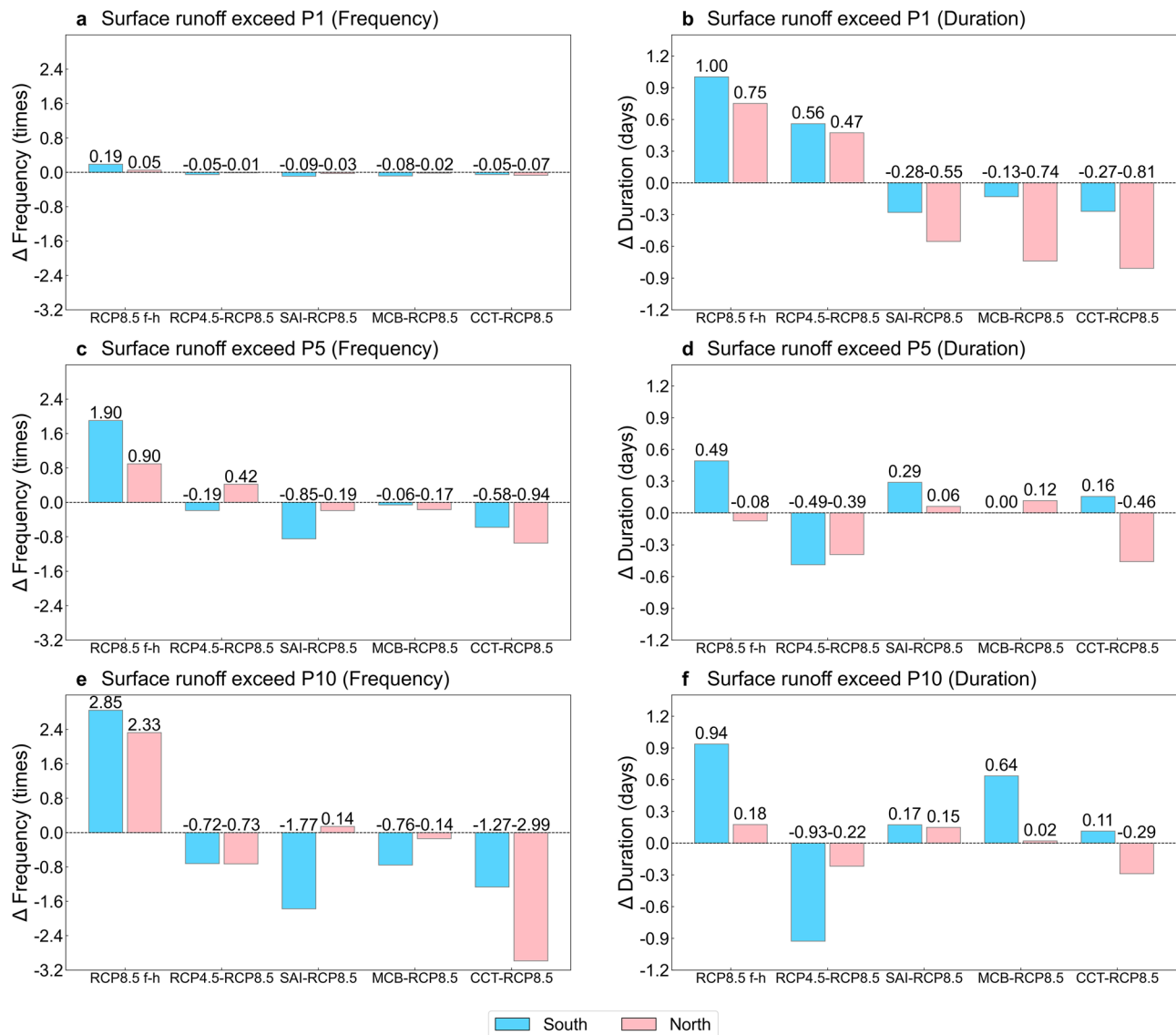


Fig. 4 | The projected differences in extreme runoff events between different scenarios in northern and southern monsoon regions. a, b Changes in the frequency and duration of P1 events (recurrence interval of 100 years); **c, d** Changes in the frequency and duration of P5 events (recurrence interval of 20 years); **e, f** Changes in the frequency and duration of P10 events (recurrence interval of 10

years). Values on the bars are changes between late 21st century (2070–2099) and early 21st century (2006–2035) under RCP8.5 (referred as RCP8.5 (f–h)), and differences of RCP4.5, SAI, MSB, and CCT compared to RCP8.5 (referred as RCP4.5–RCP8.5, SAI–RCP8.5, MCB–RCP8.5, CCT–RCP8.5), respectively, at the end of the 21st century (2070–2099).

monsoon regions are projected to experience a decrease in P1 event frequency under all SRMs and RCP4.5, while changes in event duration are more regionally variable.

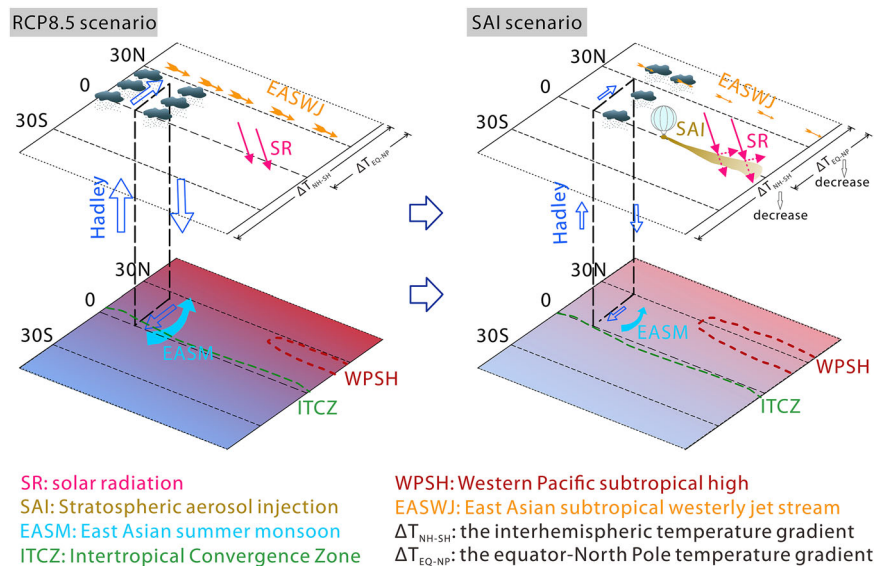
Mechanisms of atmospheric dynamics driving runoff changes

Under RCP8.5, the projected increases in precipitation and ET in late 21st century (Supplementary Fig. 13) are driven by increased water vapor (see increased 850 hPa specific humidity in Supplementary Fig. 14) from rising temperatures and intensified East Asian monsoons³⁶ (see increased 850 hPa southwesterly wind in Supplementary Fig. 15d) due to atmospheric thermodynamic and circulation changes^{37,38}. These changes result in increased precipitation across the monsoon regions³⁰, but intensified NDSF pattern for runoff, particularly in summer (Supplementary Fig. 13). While global warming also intensifies the East Asian winter monsoon^{39,40} (see strengthened northerly winds in Supplementary Fig. 15j), projected changes in winter precipitation and runoff are relatively modest (Supplementary Fig. 13).

Under SRM scenarios, reduced temperatures alter atmospheric circulation patterns, leading to distinct regional changes in the hydrological

cycle. In our simulations, SAI mitigates the NDSF precipitation pattern compared to RCP8.5, primarily by reducing inter-hemispheric (ΔT_{NH-SH} , Supplementary Fig. 16) and equator-to-North-pole (ΔT_{EQ-NP} , Supplementary Figs. 17–19) temperature gradients (see Methods section “Diagnostics”). The ΔT_{NH-SH} is crucial in regulating the latitudinal position of the planetary atmospheric circulation^{41–43}, including the Hadley circulation terminus and Intertropical Convergence Zone (ITCZ). When the ΔT_{NH-SH} decreases, the ITCZ shifts southward as reported in another SAI study⁴³, leading to a weakening of the East Asian summer monsoon (EASM)⁴⁴ and reduced intensity of precipitation across the monsoon regions. Sea surface temperature decreases over the ITCZ would weaken the Hadley circulation⁴⁵. Simultaneously, a reduction in the upper level ΔT_{EQ-NP} would reduce Hadley cell intensity and also suppress baroclinic wave activity, enabling angular momentum conservation to extend farther toward the North pole⁴⁶. The weakening of upper level ΔT_{EQ-NP} would inhibit the generation and development of synoptic baroclinic disturbances, limiting the kinetic energy transfer from transient eddies to the mean flow, which in turn weakens the East Asian subtropical westerly jet (EASWJ)^{47,48}. The

Fig. 5 | Schematic diagram showing the mechanisms of SAI in adjusting the NDSF conditions over China. Comparison of atmospheric conditions under SAI (right) to the reference condition (RCP8.5, left) reveals a series of cascading effects on the atmospheric circulation and the East Asian summer monsoon system: (1) the implementation of SAI reduces both ΔT_{NH-SH} and ΔT_{EQ-NP} (see their calculations in Methods section “Diagnostics”); (2) the weakened ΔT_{NH-SH} leads to the southward shift of the ITCZ and a weakening of the EASM; (3) the weakened ΔT_{EQ-NP} and surface temperature over tropical suppresses the Hadley circulation, weakening the EASWJ and prompting the northward movement of WPSH, as well as the northward shift of the WPSH, resulting in increased (decreased) precipitation in the north (south) of China.



reduction in the ΔT_{EQ-NP} eventually lead to the weakening of EASWJ and its northward shift associated with the expansion of the Hadley circulation⁴⁹, resulting in a northward shift of summer rainfall towards northern China⁵⁰. The northward shift of the EASWJ can also align with the northward shift of the western Pacific subtropical high (WPSH), often during La Niña development. Their combined shifts typically bring positive rainfall anomalies to northern China⁵¹.

The above mechanisms can explain the simulated SAI-induced NDSF changes, which are illustrated in Fig. 5. Under RCP8.5 scenario, the unabated warming leads to a pronounced increase in ΔT_{NH-SH} across tropospheric levels (Supplementary Fig. 20), accompanied by intensified ΔT_{EQ-NP} at upper troposphere (300 hPa, Supplementary Fig. 21). These thermal gradient changes strengthen the summer monsoon circulation (enhanced 850 hPa winds, Supplementary Fig. 15d) and drive southward displacements of the EASWJ (Supplementary Fig. 15f) and the ridge line of WPSH (Supplementary Fig. 22), resulting in more precipitation in the south (Supplementary Fig. 13).

In the specific condition of equatorial injections, SAI reduces ΔT_{NH-SH} in the troposphere (Supplementary Fig. 16), leading to weakened summer monsoon overall (see reduced 850 hPa wind velocity in Supplementary Fig. 23d, wind direction reversed compared to Supplementary Fig. 15d). The weakening of the meridional temperature gradient in the lower troposphere is widely predicted to induce an equatorward shift of the EASWJ⁵², while a similar weakening in the upper troposphere generates a competing effect that drives the jet poleward⁴⁷. This dynamic interplay creates what is commonly referred to as the “tug-of-war” pattern^{53–55} within the jet stream system. The observed reduction in ΔT_{EQ-NP} at upper troposphere (300 hPa, Supplementary Fig. 17) and relatively stable lower tropospheric gradients in subtropics (Supplementary Figs. 18, 19), together with enhanced meridional temperature gradient on the poleward side which push the EASWJ northward⁵⁶, ultimately drives a northward displacement of the EASWJ in this “tug-of-war” pattern between latitudinal thermal contrasts in SAI. Reduction of surface temperature (Supplementary Fig. 24) induces weakened Hadley circulation, which further supports the northward shift of EASWJ. The combined weakening (Supplementary Fig. 25f) and poleward displacement of the EASWJ, characterized by particularly pronounced zonal wind reductions in southern regions (Supplementary Fig. 23f), along with the concurrent northward migration of the ridge line of WPSH (Supplementary Fig. 26), collectively drive a dipole precipitation response during the summer monsoon season. These circulation changes are expected to bring increased (decreased) precipitation to the north (south) during the summer monsoon compared to RCP8.5 (Supplementary

Figs. 6b, 30f). Moreover, SAI induces greater reductions in 850 hPa specific humidity in southern monsoon regions than the north during spring and summer (Supplementary Fig. 14), further mitigating NDSF.

The ΔT_{NH-SH} changes in MCB and CCT are similar to that in SAI at 850 hPa and 300 hPa, which are all decreases compared to RCP8.5 (Supplementary Fig. 16). But at 500 hPa, MCB and CCT show a marginal increase (less than 0.001 °C for MCB and 0.03 °C for CCT), which lead to an enhanced summer monsoon (increased wind velocity; Supplementary Figs. 34d and 35d). The stronger weakening of ΔT_{EQ-NP} at both upper and middle upper troposphere under MCB (Supplementary Figs. 17, 18) causes greater northward displacements of the WPSH (Supplementary Fig. 27) and the EASWJ (Supplementary Figs. 34f) compared to SAI. Combined with enhanced water vapor depletion over 10°N–35°N (Supplementary Fig. 14n), this results in reduced summer precipitation over the northern monsoon region despite intensified summer monsoon. In contrast to its summer position, the autumn EASWJ shifts southward (Supplementary Fig. 34f, i), together with slightly increased water vapor (Supplementary Fig. 14o), driving an associated southward movement of the precipitation belt (Supplementary Fig. 31j). Although the weakened ΔT_{EQ-NP} under CCT leads to northward movement of WPSH (Supplementary Fig. 28) along with EASWJ attenuation (Supplementary Fig. 25h), a bifurcation structure is unexpectedly induced over northeastern China (Supplementary Fig. 35f), together with even less water vapor over China (Supplementary Fig. 14r), resulting in decreased precipitation in the northern region.

RCP4.5 produces identical ΔT_{NH-SH} and ΔT_{EQ-NP} evolution patterns closely resemble those in SAI, which drive similar summer monsoon modifications (Supplementary Figs. 29 and 36d) and precipitation pattern (Supplementary Fig. 33f). Less precipitation over the north under RCP4.5 compared to that under SAI is due to the greater reduction in specific humidity (Supplementary Fig. 14f).

The variation in relative vorticity would impact convective rainfall during summer monsoon. Under SAI and RCP4.5, the decrease in relative vorticity in the south, particularly the Yangtze River basin (Supplementary Figs. 23e and 36e), also suppresses convective rainfall there during the summer. The decrease of surface pressure (Supplementary Fig. 37) over west of China contribution to the upward vertical motion in the airflow (Supplementary Fig. 38), together with the increase in relative vorticity (Supplementary Figs. 23e, 34e, 35e, and 36e) which will induce convection and positive rainfall anomalies (Supplementary Figs. 30f, 31f, 32f, and 33f) over west China.

All SRM scenarios and RCP4.5 exert weaker influences on the winter monsoon compared to their substantial impacts on the summer monsoon,

causing smaller changes in precipitation and runoff in winter. An exception is MCB, where the 850 hPa specific humidity increases along the coast region over southern China (Supplementary Fig. 14p), which could explain increased winter precipitation in the south (Supplementary Fig. 31n).

Moreover, these SRM scenarios and RCP4.5 cause more severe reductions in summer (JJA) specific humidity (Supplementary Fig. 14) throughout China and more heterogeneous contribution of ET to runoff changes (Supplementary Figs. 30–33). Consequently, their net climate effects on surface runoff are uniformly positive (MCB, RCP4.5) or negative (CCT) across northern and southern monsoon regions (Table 1), which would exacerbate either flooding in the south or drought in the north in these simulations.

Underlying thermodynamic mechanisms

Warming of the stratosphere and cooling of the troposphere are observed in three SRM scenarios and RCP4.5 (Supplementary Fig. 39). Under SAI, a pronounced anomalous warming occurs in the tropical lower stratosphere, with the magnitude of warming progressively decreasing toward higher latitudes. Conversely, in the troposphere, maximum cooling is observed in tropical regions (due to the equatorial injection of our SAI design), with the cooling effect diminishing poleward and eventually transitioning to warming at higher latitudes. MCB produces tropical temperature responses broadly similar to SAI, except with weaker lower-stratospheric warming and stronger tropospheric cooling. CCT induces maximum tropospheric cooling in tropical regions, coupled with relatively weak lower-stratospheric warming. In contrast, it produces the strongest warming at high latitudes among all SRM scenarios. Under RCP4.5, stratospheric warming exhibits a distinct vertical gradient, with the magnitude of temperature increase growing progressively with altitude. This contrasts with the tropospheric cooling pattern, which shows spatial similarities to that of SAI.

The hemispheric asymmetry in tropospheric cooling (Supplementary Figs. 40–42) over subtropical and middle latitude region (30°N–40°N) constitutes a critical driver of modified meridional temperature gradients, ultimately reshaping the EASWJ and the position of rain belt. Under SAI, the negative anomalies in atmospheric radiative flux (Supplementary Fig. 43f) around 30°N induce tropospheric cooling (especially at upper level–300 hPa) through reduced diabatic heating. This is fundamentally linked to SAI-induced cloud modifications (Supplementary Fig. 46), particularly through reduced mid-to-upper level clouds in these regions. The diminished cloudiness reduces shortwave reflection (Supplementary Fig. 44f) and enhances net longwave cooling (Supplementary Fig. 45f), collectively contributing to the observed upper-tropospheric temperature decrease.

More pronounced hemispheric cooling asymmetry induced by MCB (Supplementary Figs. 40g, 41g, and 42g) amplifies meridional temperature gradient anomalies. This results in more substantial modifications to the northward move of EASWJ (see above section). This may be related to the reduced clouds (Supplementary Fig. 47e–h) across all vertical levels (low/middle/high) over the tropical-to-subtropical Northwest Pacific, which enhance the net longwave cooling (Supplementary Fig. 45g) while reduce shortwave reflection (Supplementary Fig. 44g) more than in SAI, leading to stronger temperature decreases—particularly in the mid-to-upper troposphere. Although CCT produces the most pronounced hemispheric cooling asymmetry among SRM scenarios, its spatial structure—characterized by stronger temperature reductions at more southwesterly locations—induces a distinct directional shift in the EASWJ. CCT induces the most substantial high-level cloud reduction (Supplementary Fig. 48e) in tropical regions among the SRM scenarios, generating the strongest net longwave cooling (Supplementary Fig. 45h) and the most pronounced shortwave reflection reduction (Supplementary Fig. 44h). The cloud dynamical responses under RCP4.5 (Supplementary Fig. 49) exhibit striking similarities to those under SAI, which generate comparable hemispheric cooling asymmetry patterns through analogous cloud-radiative feedback.

Evidence from the Mount Pinatubo volcanic eruption

We further validate the reliability of the mechanism (Fig. 5) proposed here by examining the impact of the 1991 Mount Pinatubo volcanic eruption, a real-world analogue of near-equatorial SAI, on precipitation in China (Fig. 6). Ref. 57 suggested that the 1991 Mount Pinatubo eruption increased precipitation during the first half of July in the Yangtze-Huaihe River basins (YHRB) of China by intensifying the rainband north of the cold Maritime Continent and strengthening the WPSH (Fig. 6f). The internal climate variabilities, including the preceding winter El Niño (Nino3.4) warm anomaly, fall Dipole mode index (DMI) positive anomaly, and spring North Atlantic Oscillation (NAO) negative anomaly that typically enhance summer precipitation over East China⁵⁸ were all weakened in 1991 (Fig. 6a), which demonstrates the potential role of this eruption (June 15th, 1991) in the extreme YHRB precipitation anomaly (Fig. 6a, f). The northward migration of the WPSH in July (Fig. 6f, g), along with the typical northward shift of the East Asian rainband (Fig. 6f, g) during the same period, are well-established climatological patterns²¹. The $\Delta T_{\text{EQ-NP}}$ in 1991 experienced a more pronounced decreasing trend between the two periods following the eruption (June 29th to July 15th and July 16th to July 31st) in 1991 compared to the corresponding climatological difference of the two periods (bars in Fig. 6b–d). After mid-July in 1991, the tropics were covered by thicker stratospheric volcanic aerosols⁵⁷. This leads to a smaller increase of $\Delta T_{\text{NH-SH}}$ in the lower to upper troposphere (Fig. 6e) during July 16th to July 31st in 1991, resulting in a weakened EASM compared to the climatology (see wind field in Fig. 6g), similar to our simulated effects of SAI (Supplementary Fig. 23d). The substantially stronger reduction in $\Delta T_{\text{EQ-NP}}$ during July 16th to July 31st causes the WPSH and rainband to shift northward, resulting in increased precipitation in the north and decreased precipitation in the south, similar to the above mechanism for SAI (Fig. 5). The weakened EASM during this period resulted in weaker, but positive precipitation anomalies (Fig. 6g) reaching the north. Although the Mount Pinatubo eruption had weaker radiative forcing than the simulated equatorial SAI at the end of 21st century, its impact on the monsoon's mean-state response and the mechanisms of how they change the NDSF precipitation pattern in China's monsoon regions are largely consistent.

Discussion

Our results demonstrate that different climate intervention approaches could have distinct impacts on China's monsoon and NDSF pattern, with important implications for regional water resource management. The identification of a clear mechanism through which equatorial SAI could modify this characteristic dry-wet pattern represents a major advance in understanding how climate interventions might affect regional hydroclimate. By reducing both inter-hemispheric and equator-to-north-pole temperature gradients, SAI induces systematic changes in atmospheric circulation and the monsoon system, including the weakening and expansion of the Hadley circulation, northward movement of the EASWJ and northward shift of the WPSH. These changes collectively increase precipitation and surface runoff in northern China while reducing them in the south, thereby mitigating the longstanding NDSF water imbalance issue in our high-emissions background scenario and deployment strategy. The consistency between model projections and observed precipitation changes following the 1991 Mount Pinatubo eruption provides crucial real-world validation of this mechanism.

Furthermore, our results reveal potential trade-offs between global climate intervention efficacy and regional water resource distribution. While all interventions investigated here achieve similar cooling, their divergent effects on the monsoon system and surface runoff highlight the complexity of regional hydroclimatic responses to large-scale forcing. Although equatorial SAI shows potential for mitigating NDSF, the intensification of flood or drought risks in different regions under MCB, CCT, and RCP4.5 scenarios (relative to RCP8.5) indicates that the choice and design of intervention strategy could have profound implications for

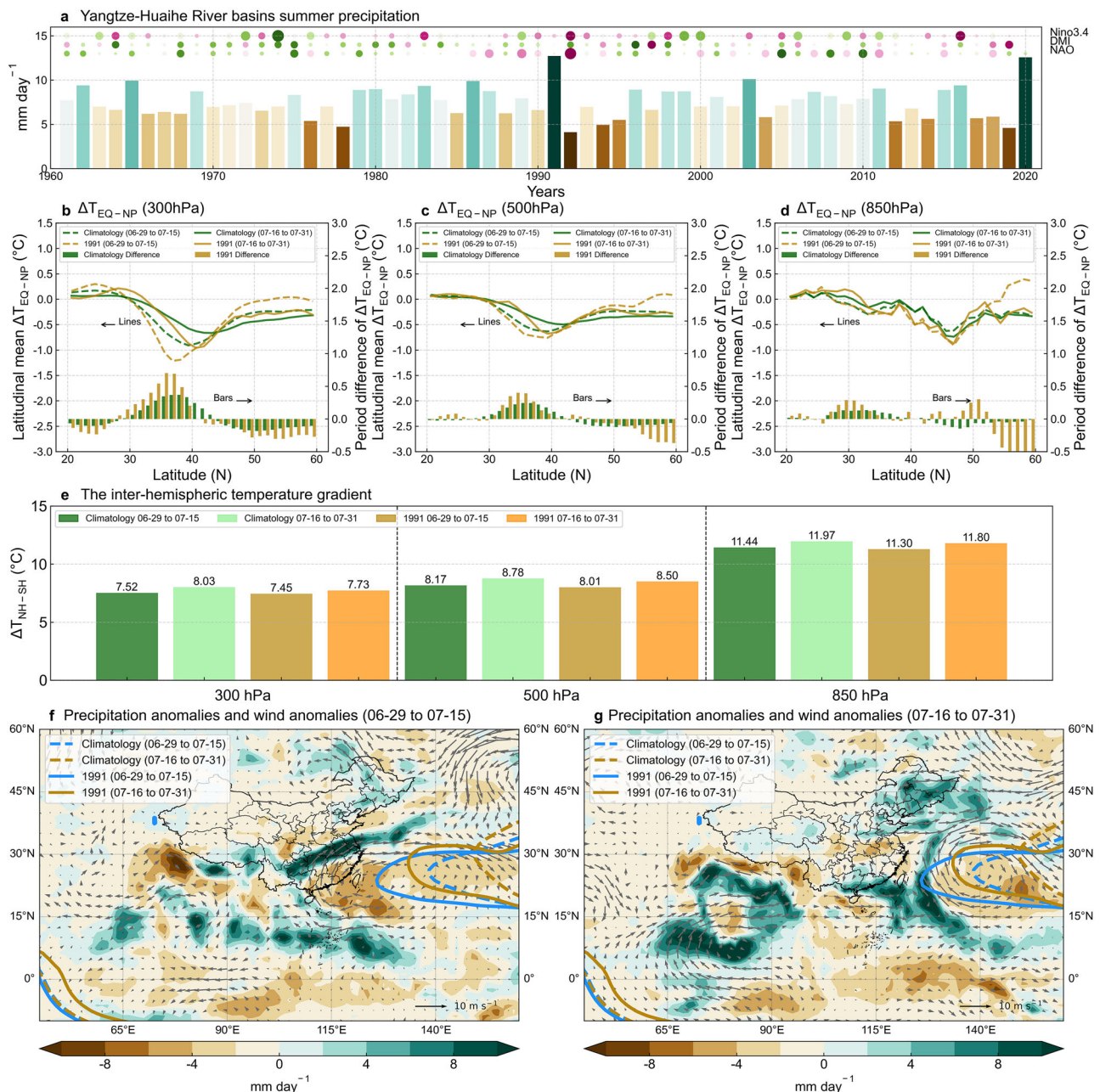


Fig. 6 | Observed precipitation anomalies in China after 1991 Mount Pinatubo volcanic eruption. **a** Summer precipitation of the Yangtze-Huaihe River basins. Colored dots, where warm colors indicate positive values and cool colors indicate negative ones, represent the preceding winter Nino3.4 index, fall Dipole mode index (DMI), and spring North Atlantic Oscillation (NAO) index, in order. The size of each dot corresponds to its strength. **b–d** The latitudinal mean equator-to-North pole temperature gradient (ΔT_{EQ-NP}) of two periods June 29th–July 15th (dashed lines) and July 16th–July 31st (solid lines) of 1991 following the Mount Pinatubo volcanic eruption (yellow lines) and the corresponding daily climatology of 1961–2020 for the two periods (green lines, left Y-axis), at 300 hPa (**b**), 500 hPa (**c**),

850 hPa (**d**), respectively. Bars represent the difference of latitudinal mean ΔT_{EQ-NP} between the two periods (June 29th–July 15th and July 16th–31st) in 1991 (yellow bars) and corresponding climatological difference (green bars, right Y-axis). Calculation of ΔT_{EQ-NP} is focused on the East Asian sector (see “Methods” section “Diagnostics”). **e** The inter-hemispheric temperature gradient (ΔT_{NH-SH}) at 300 hPa, 500 hPa, and 850 hPa of the two periods. Precipitation and wind anomalies of the two periods June 29th–July 15th (**f**) and July 16th–July 31st (**g**) in 1991 relative to their corresponding climatology. The four lines in **f** and **g** are the average WPSH at 850 hPa for the two periods June 29th–July 15th (blue) and July 16th–July 31st (yellow) of 1991 (solid lines) and the corresponding climatology (dashed lines).

regional water security. The differing impacts of MCB and CCT compared to SAI stem not only from the type of SRM but also from their distinct spatial forcing patterns and cloud-humidity feedbacks. SAI produces relatively uniform tropical forcing via stratospheric aerosols, whereas MCB introduces zonal asymmetry by targeting chosen ocean regions, leading to regionally concentrated surface cooling and stronger meridional temperature gradients. CCT, affecting longwave radiation by thinning cirrus clouds, alters upper-tropospheric cooling and stability in ways that differ from

shortwave-based interventions. Both MCB and CCT also cause greater reductions in lower-tropospheric humidity, limiting precipitation despite changes in circulation. These differences help explain why MCB increases southern flood risk, and CCT worsens northern drought, unlike the more balanced response seen under SAI. These findings underscore the importance of incorporating regional hydrological impacts in the evaluation and design of climate interventions, particularly for regions with strong spatial gradients in water availability.

The NDSF precipitation pattern has prevailed in eastern China during most warm periods over the past 2000 years²⁵. Throughout the Holocene, however, there existed a dipolar mode of precipitation anomalies—“north drought (flood)–south flood (drought)” (NDSF/NFSD), with NFSD prevailing in the middle Holocene and NDSF in the early and late Holocene⁵⁹. These historical reversals, while not contradicting the current dominance of NDSF, help illuminate the mechanism of hydrological changes under an altered climate of SAI. Studies⁶⁰ have attributed the dipolar mode in the Holocene to the influence of El Niño/Southern Oscillation (ENSO). During the middle Holocene, La Niña-like conditions caused the WPSH to retreat northeastward, shifting the rain belt northward and creating the NFSD pattern, while El Niño-like conditions produced the typical NDSF. For equatorial SAI or near-equatorial volcanic eruptions (like Mount Pinatubo in 1991), the weakening of atmospheric thermodynamics and the cooling of the troposphere led to reduced $\Delta T_{\text{NH-SH}}$ and $\Delta T_{\text{EQ-NP}}$ (along with La Niña-like sea surface temperature anomalies), which can trigger a cascade of circulation shifts in the ITCZ, EASWJ and WPSH that mirror those observed during the middle Holocene NDSF-to-NFSD transition. The resulting distinct south–north disparity in precipitation changes is key to counteracting the NDSF pattern in China’s monsoon regions. This paleoclimate perspective reinforces our mechanistic understanding of SAI’s regional impacts, calling for careful intervention design based on circulation patterns.

Some caveats are warranted. Our results could be deployment strategy dependent, as well as model dependent and should be validated by further studies. Our use of the NorESM1-ME model ensures a consistent framework for simulating all three SRM scenarios, though model-specific uncertainties remain (see “Methods”: “Model performance evaluation”). In the future, updated versions of this model, such as NorESM2⁶¹, including the improved hydrological processes in its land component CLM5⁶², can be utilized to improve simulation capabilities, and multiple Earth system models can be employed to further examine the impact of climate interventions, especially SAI, on the regional hydrological cycle and water resource patterns. Although the model used has known biases that may affect the magnitude and spatial detail of projected changes, the overall north–south runoff contrast is likely robust. Similar patterns of circulation and precipitation changes observed after the 1991 Mount Pinatubo eruption clearly support the mitigation mechanism of equatorial SAI on China’s NDSF. More experiments can be conducted to compare the effects of different SAI injection methods⁶³ on the distribution of water resources in China and other regions of the world. We note that numerous other factors can influence the East Asia monsoon system⁶⁴ and water resource distribution. This paper focuses on a few of the most evident aspects of atmospheric physics and land surface feedbacks to analyze the mechanisms of SAI’s impact on surface runoff. More aspects of the water cycle and human activities should be taken into account to fully understand the impacts of SRMs and emissions reduction on water resource availability.

We acknowledge that there are many degrees of freedom when designing the SRM scenarios, e.g., based on the spatio-temporal distributions of the implemented forcing patterns, which would lead to yield distinct rainfall responses^{65–67}. Nevertheless, the aim of our study is to elucidate key changes in the regional hydrological cycles in response to fundamentally distinct SRM forcings. Notably, the mechanism by which SAI mitigates NDSF—through weakening the inter-hemispheric and meridional temperature gradients ($\Delta T_{\text{NH-SH}}$ and $\Delta T_{\text{EQ-NP}}$)—depends strongly on equatorial aerosol injection in our specific SAI design. This aligns with other SAI studies using different models^{68,69}, which report similar north (increase)–south (decrease) disparities in precipitation changes over eastern China under equatorial or near-equatorial injections but not under mid- or high-latitude injections. Future studies that explore impacts of different injection designs of each SRM method on regional climate would be valuable.

Overall, SAI is one of the most well-studied SRM proposals, theoretically capable of quickly mitigating global warming while providing the necessary transition time to achieve emissions reduction goals. We show that in our model design and with these scenarios, equatorial SAI can

provide a more balanced and sustainable hydroclimatic environment for China’s water resource management. However, it should be noted that SAI and other forms of climate intervention are not to be considered as substitutes for emission reductions, considering that such interventions do not address the root cause of anthropogenic climate change and may introduce novel climatic features with consequences on other components of the Earth system⁷⁰. To better evaluate the potential of SRM strategies for addressing climate change alongside emissions reduction, the climate research community should continue to undertake more comprehensive investigations, including their regional implications, tradeoffs, ethical and governance challenges.

Methods

Model and SRM design

We used the fully coupled, emission-driven Norwegian Earth System Model version 1 (NorESM1-ME)³², a CMIP5-era Earth system model with established capabilities for simulating stratospheric aerosol processes and multiple SRM methods. Despite the availability of CMIP6 models, NorESM1-ME remains among the few with integrated modules for SAI, MCB, and CCT within a consistent framework. NorESM1-ME offers a well-tested platform for evaluating SRM impacts on regional hydroclimates^{13,71,72}. We used three SRM deployment scenarios (SAI, MCB, and CCT) for the period of 2020–2099 and two reference climate scenarios (RCP4.5 and RCP8.5) for the same period. The SAI experiment only considered equatorial SAIs, with specified sulfate aerosol concentrations and distributions, taken from the ECHAM5 model⁷³. The distribution of the aerosol optical depth is described in ref. 74. The MCB was implemented in the model by increasing accumulation mode sea salt emissions over the ocean surface in the latitude range of 45° North and South. The accumulation mode is equivalent to a dry number modal radius of 0.13 μm for sea salt in the model. The CCT was simulated by increasing the terminal velocity of ice crystals in the atmosphere where temperatures are below -38°C . More details of these SRM implementations can be found in ref. 13 (see summary and nomenclature in Supplementary Table 1). Each experiment was conducted in three realizations by introducing perturbations to the initial conditions at the beginning of every simulation¹³. Our experiments represent a unique set for comparison of the three SRM scenarios consistently designed to have a trajectory of net radiative forcing comparable to that of GHG emissions reduction from the RCP8.5 to RCP4.5 scenarios. Although all SRM scenarios were designed to offset the radiative forcing of RCP8.5 to approximate RCP4.5 levels, differences in implementation strategy led to distinct spatial forcing patterns. SAI uses equatorial stratospheric sulfate injections, producing relatively uniform tropical forcing. In contrast, MCB targets low-level marine clouds in midlatitudes, introducing zonal asymmetry and greater regional variability. CCT modifies high-altitude ice cloud properties globally, primarily affecting longwave radiation. These differences, while controlled for in terms of global radiative forcing, may lead to divergent regional climate responses. All the simulations were run at a resolution of 1.9° latitude by 2.5° longitude and a temporal resolution of 30 min in the land and atmosphere.

Model performance evaluation

To assess the model’s performance over China, we compared NorESM1-ME simulated monthly surface runoff, total precipitation, and ET under RCP8.5 with observations, reanalysis and data from CMIP6. Comparison with ERA5 reanalysis data⁷⁵ during the historical period 2006–2020 (Supplementary Fig. 50) shows a coefficient of determination (R^2) of 0.88, 0.93, and 0.97 for monthly surface runoff, total precipitation, and ET, respectively. The root mean square errors (RMSE) for monthly surface runoff, total precipitation, and ET are 11.44, 22.22, and 11.45 mm month^{-1} , respectively. We also compared the simulated surface runoff with the China Natural Runoff Dataset (CNRD)⁷⁶, which shows R^2 of 0.86 and RMSE of 15.04 mm month^{-1} (Supplementary Fig. 51). The grid-cell-level evaluation of monthly surface runoff and climate components is presented in Supplementary Fig. 52. Compared

to ERA5 reanalysis data, the RCP8.5 simulations systematically overestimated runoff, precipitation, and ET across most regions. When validated against CNDR, the model showed contrasting biases: it underestimated runoff in southern China while overestimating northern runoff. In general, the simulation results exhibit larger maximum values and slightly lower minimum values in surface runoff than the CNRD and ERA5 reanalysis data. Despite some mismatch in the extreme values, the simulated seasonal pattern of surface runoff, total precipitation, and ET over China are in good agreement with the reanalysis. When compared with CMIP6 data, the simulated runoff changes under RCP8.5 also align with the multi-model mean projections (Supplementary Fig. 3) and published literature³³.

Diagnostics

The large-scale climatic impacts as well as changes in different components of the Earth system in these three SRMs have been evaluated in previous studies^{13,77–79}. Here, we further assess the impact of these SRMs on China's north-south water resource distribution by analyzing surface runoff and related climate data obtained from the above simulations. First, we investigated the future trends of surface runoff, total precipitation, actual ET, and surface air temperature, using the area-weighted averages for China (Supplementary Fig. 1). We also compared the changes in surface runoff and climate in China under each scenario between the late 21st century (2070–2099) and the early 21st century (2006–2035), using 30-year annual average values for comparison (Supplementary Fig. 2). For the early 21st century before the beginning of the SRM scenarios, results from the RCP8.5 scenario (2006–2019) were used to supplement the data, noting also small differences between the RCPs in these early years of the scenarios. To assess the effects of different SRMs and emissions reduction (RCP4.5) scenarios, we compared surface runoff characteristics during 2070–2099 under SAI, MCB, CCT and RCP4.5 to that of RCP8.5 (Fig. 2). The resulting differences of SAI-RCP8.5, MCB-RCP8.5 and CCT-RCP8.5 represent SRM effects, whereas RCP4.5-RCP8.5 represents a set of effects, encompassing emissions reduction, land use changes, and other factors (emissions reduction for short, because our attribution analysis shows minor land use change effects on runoff; see Supplementary Note 2 and Supplementary Tables 3–4). We paid particular attention to hydroclimatic changes in the relatively drier northern and wetter southern parts (Fig. 2, Supplementary Figs. 6–8) of China's monsoon region, that is, north-drought and south-flood regions, consistent with the characteristic NDSF precipitation pattern²⁶ (see Fig. 1 for details). The effects of SRMs and RCP4.5 on the NDSF water divide were then evaluated relative to RCP8.5. We conducted 95% two-sided U-tests to determine statistical significance.

Furthermore, we examined changes in water availability under extreme conditions. We analyzed the frequency and duration of daily surface runoff exceeding a certain threshold that defines extreme events. We considered the 30-year climatological average of surface runoff for each calendar day under the RCP8.5 from 2070 to 2099 as the baseline condition. We used Pearson-III curve fitting⁸⁰ to generate frequency distribution curves and determined the surface runoff at recurrence intervals of 10, 20, and 100 years for extreme analysis (Supplementary Figs. 9–12, Fig. 4). These recurrence intervals correspond to the probabilities of 10% (P10), 5% (P5), and 1% (P1), respectively.

Third, we investigated the drivers for changes in surface runoff under the different scenarios. We used an attribution framework developed by Zhou et al.⁸¹ to untangle the land surface and climate change effects on surface runoff changes (Table 1, Supplementary Tables 2–4). The attribution method, known as the complementary method, was derived from the Budyko complementary relationship⁸². The Choudhury–Yang equation^{83,84} was adopted as the Budyko model, and the reference crop Penman–Monteith equation⁸⁵ was employed to calculate PET, which was used in the Budyko model. Details are described in Supplementary Note 1.

Finally, we analyzed the impacts of SRMs on atmospheric circulation patterns and the East Asian monsoon by examining annual and seasonal changes in surface runoff and climate variables (temperature, precipitation,

specific humidity, wind, geopotential height, radiation, cloud, etc.) compared to RCP8.5 (Supplementary Figs. 13–49). We calculated the inter-hemispheric temperature gradient (ΔT_{NH-SH}) at three levels (300 hPa, 500 hPa, and 850 hPa) as the difference in area-weighted average temperatures between the Northern and Southern Hemispheres (Due to data availability issues at 850 hPa, the calculation of temperature differences was limited to latitudes between 70°S and 70°N to ensure robust results.). The equator-to-North-pole temperature gradient (ΔT_{EQ-NP}) at three levels was calculated within the East Asian sector (100°E–150°E) from 10°N to 60°N by computing the meridional temperature gradient (that is, the mean temperature difference between adjacent latitude bands) along each longitude. We then summarized the mechanism by which SAI mitigates the NDSF pattern in China (Fig. 5). Additionally, we further demonstrate the validity of this mechanism by analyzing observed anomalies of circulation patterns and precipitation in two adjacent periods (June 29th–July 15th and July 16th–July 31st) after the 1991 Mount Pinatubo volcanic eruption, which is analogous to near-equatorial deployment of SAI and shows similar effects on circulation and precipitation (Fig. 6).

Three pressure levels (300 hPa, 500 hPa, and 850 hPa) at troposphere are chosen for their representative roles in the EASM circulation system^{21,86}, which have been used in previous studies of geoengineering^{17,18}. In particular, 300 hPa is selected to assess upper-tropospheric temperature gradients and jet stream dynamics, as it corresponds to the core altitude of the EASWJ, which plays a key role in modulating summer monsoon rainfall^{87–89}. This level is also where SAI-induced stratosphere–troposphere coupling is most evident, especially given its proximity to the lower stratosphere where aerosols modify radiative heating⁹⁰. Studies have shown that both observed and modeled shifts in the EASWJ under climate change or geoengineering scenarios are strongly associated with upper-tropospheric temperature gradient changes at or near 300 hPa^{48,91–93}. Changes in thermal gradients at this altitude directly influence the strength and position of the jet, which in turn affects large-scale moisture transport and convective activity across East Asia. Thus, our analysis at this level provides a physically motivated indicator of circulation-driven hydroclimatic changes.

Reporting summary

Further information on research design is available in the Nature Portfolio Reporting Summary linked to this article.

Data availability

The post-processed data that support the findings of this study are available on Zenodo (<https://doi.org/10.5281/zenodo.16792015>)⁹⁴. The global daily precipitation, temperature, and wind for the volcanic analysis were obtained from the Japanese Reanalysis for Three Quarters of a Century (JRA-3Q)⁹⁵. The monthly Nino3.4 index was obtained from <https://psl.noaa.gov/data/timeseries/month/>. The monthly North Atlantic Oscillation (NAO) index was obtained from <https://www.cpc.ncep.noaa.gov/products/precip/CWlink/pna/norm.nao.monthly.b5001.current.ascii.table>. The monthly Indian Ocean DMI was obtained from <https://psl.noaa.gov/data/timeseries/month/DMI/>. The CMIP6 model data used for comparison of surface runoff and total precipitation with NorESM1-ME in this study were obtained from the Earth System Grid Federation (ESGF) nodes (<https://esgf-node.llnl.gov/>). The data for model performance evaluation include ERA5 reanalysis data⁷⁵ from the European Centre for Medium-Range Weather Forecasts (ECMWF) and the China Natural Runoff Dataset (CNRD)⁷⁶.

Code availability

NorESM1-ME is available at <https://github.com/NorESMhub/NorESM>. Figures were generated using Python 3.11.8, ArcGIS 10.7 and CorelDRAW 2021. The code used to produce the figures is available on Zenodo (<https://doi.org/10.5281/zenodo.16792015>)⁹⁴.

Received: 25 March 2025; Accepted: 15 August 2025;

Published online: 04 September 2025

References

- Hansen, J. E. et al. Global warming has accelerated: are the United Nations and the public well-informed? *Environment* **67**, 6–44 (2025).
- Gambhir, A. et al. Near-term transition and longer-term physical climate risks of greenhouse gas emissions pathways. *Nat. Clim. Change* **12**, 88–96 (2022).
- Ming, T., de Richter, R., Liu, W. & Caillol, S. Fighting global warming by climate engineering: is the Earth radiation management and the solar radiation management any option for fighting climate change? *Renew. Sustain. Energy Rev.* **31**, 792–834 (2014).
- Visioni, D. et al. Opinion: the scientific and community-building roles of the geoengineering model intercomparison project (GeoMIP)—past, present, and future. *Atmos. Chem. Phys.* **23**, 5149–5176 (2023).
- Ricke, K., Wan, J. S., Saenger, M. & Lutsko, N. J. Hydrological consequences of solar geoengineering. *Annu. Rev. Earth Planet. Sci.* **51**, 447–470 (2023).
- Tan, M. L., Juneng, L., Kuswanto, H., Do, H. X. & Zhang, F. Impacts of solar radiation management on hydro-climatic extremes in Southeast Asia. *Water* **15**, 1089 (2023).
- Usha, K. H., Bala, G. & Xavier, A. Sensitivity of the global hydrological cycle to the altitude of stratospheric sulphate aerosol layer. *Environ. Res. Lett.* **19**, 84024 (2024).
- McLaren, D. & Corry, O. Solar geoengineering research faces geopolitical deadlock. *Science* **387**, 28–30 (2025).
- Bala, G., Duffy, P. B. & Taylor, K. E. Impact of geoengineering schemes on the global hydrological cycle. *Proc. Natl. Acad. Sci. USA* **105**, 7664–7669 (2008).
- Irvine, P. J. & Keith, D. W. Halving warming with stratospheric aerosol geoengineering moderates policy-relevant climate hazards. *Environ. Res. Lett.* **15**, 044011 (2020).
- Ji, D. et al. Extreme temperature and precipitation response to solar dimming and stratospheric aerosol geoengineering. *Atmos. Chem. Phys.* **18**, 10133–10156 (2018).
- Latham, J. et al. Marine cloud brightening. *Philos. Trans. R. Soc. A.* **370**, 4217–4262 (2012).
- Muri, H. et al. Climate response to aerosol geoengineering: a multimethod comparison. *J. Clim.* **31**, 6319–6340 (2018).
- Muri, H., Kristjánsson, J. E., Storelvmo, T. & Pfeffer, M. A. The climatic effects of modifying cirrus clouds in a climate engineering framework. *JGR Atmos.* **119**, 4174–4191 (2014).
- Gasparini, B., McGraw, Z., Storelvmo, T. & Lohmann, U. To what extent can cirrus cloud seeding counteract global warming? *Environ. Res. Lett.* **15**, 054002 (2020).
- Zhao, M. & Cao, L. Regional response of land hydrology and carbon uptake to different amounts of solar radiation modification. *Earth's Future* **10**, e2022EF003288 (2022).
- Liu, Z., Lang, X., Miao, J. & Jiang, D. Impact of stratospheric aerosol injection on the east asian winter monsoon. *Geophys. Res. Lett.* **50**, e2022GL102109 (2023).
- Liu, Z., Lang, X. & Jiang, D. Impact of stratospheric aerosol injection geoengineering on the summer climate over East Asia. *JGR Atmos.* **126**, e2021JD035049 (2021).
- Tilmes, S. et al. CESM1(WACCM) stratospheric aerosol geoengineering large ensemble project. *Bull. Am. Meteorol. Soc.* **99**, 2361–2371 (2018).
- Kravitz, B. et al. Climate model response from the geoengineering model intercomparison project (GeoMIP). *JGR Atmos.* **118**, 8320–8332 (2013).
- Yihui, D. ing & Chan, J. C. L. The East Asian summer monsoon: an overview. *Meteorol. Atmos. Phys.* **89**, 117–142 (2005).
- Zhou, T. & Yu, R. Atmospheric water vapor transport associated with typical anomalous summer rainfall patterns in China. *J. Geophys. Res.* **110**, 2004JD005413 (2005).
- Ding, Y., Wang, Z. & Sun, Y. Inter-decadal variation of the summer precipitation in East China and its association with decreasing Asian summer monsoon. *Int. J. Climatol.* **28**, 1139–1161 (2008).
- Water Resources Management in the People's Republic of China.* <https://doi.org/10.4324/9781315875927> (Routledge, 2013).
- Zheng, J. et al. Drought/flood spatial patterns in centennial cold and warm periods of the past 2000 years over eastern China. *Chin. Sci. Bull.* **59**, 2964–2971 (2014).
- Day, J. A., Fung, I. & Liu, W. Changing character of rainfall in eastern China, 1951–2007. *Proc. Natl. Acad. Sci. USA* **115**, 2016–2021 (2018).
- Wei, K. et al. Reflections on the catastrophic 2020 Yangtze river basin flooding in Southern China. *Innovation* **1**, 100038 (2020).
- Chen, Z. & Yang, G. Analysis of drought hazards in north China: distribution and interpretation. *Nat. Hazard.* **65**, 279–294 (2013).
- You, Q. et al. Tibetan Plateau amplification of climate extremes under global warming of 1.5°C, 2°C and 3°C. *Glob. Planet. Change* **192**, 103261 (2020).
- Li, Z., Sun, Y., Li, T., Ding, Y. & Hu, T. Future changes in East Asian summer monsoon circulation and precipitation under 1.5 to 5°C of warming. *Earth's Future* **7**, 1391–1406 (2019).
- Visioni, D. et al. Identifying the sources of uncertainty in climate model simulations of solar radiation modification with the G6sulfur and G6solar geoengineering model intercomparison project (GeoMIP) simulations. *Atmos. Chem. Phys.* **21**, 10039–10063 (2021).
- Tjiputra, J. F. et al. Evaluation of the carbon cycle components in the Norwegian Earth System Model (NorESM). *Geosci. Model Dev.* **6**, 301–325 (2013).
- Zhu, X. et al. Future changes and distribution of water resources in China under global warming levels of 1.5–4.5°C. *J. Hydrol.* **53**, 101781 (2024).
- Wang, O. et al. Projected future changes in extreme precipitation over China under stratospheric aerosol intervention in the UKESM1 climate model. *Atmos. Chem. Phys.* **24**, 12355–12373 (2024).
- Kang, S. et al. Observation-constrained projection of flood risks and socioeconomic exposure in China. *Earth's Future* **11**, e2022EF003308 (2023).
- Tian, J. et al. Projections of precipitation over China based on CMIP6 models. *Stoch. Environ. Res. Risk Assess.* **35**, 831–848 (2021).
- Xu, Z., Fan, K. & Wang, H. Decadal variation of summer precipitation over China and associated atmospheric circulation after the late 1990s. *J. Clim.* **28**, 4086–4106 (2015).
- Endo, H. & Kitoh, A. Thermodynamic and dynamic effects on regional monsoon rainfall changes in a warmer climate. *Geophys. Res. Lett.* **41**, 1704–1711 (2014).
- Miao, J., Wang, T. & Chen, D. More robust changes in the East Asian winter monsoon from 1.5 to 2.0°C global warming targets. *Int. J. Climatol.* **40**, 4731–4749 (2020).
- Xu, M., Xu, H. & Ma, J. Responses of the East Asian winter monsoon to global warming in CMIP5 models. *Int. J. Climatol.* **36**, 2139–2155 (2016).
- Schneider, T., Bischoff, T. & Haug, G. H. Migrations and dynamics of the intertropical convergence zone. *Nature* **513**, 45–53 (2014).
- Routson, C. C. et al. Mid-latitude net precipitation decreased with Arctic warming during the Holocene. *Nature* **568**, 83–87 (2019).
- Cheng, W. et al. Changes in Hadley circulation and intertropical convergence zone under strategic stratospheric aerosol geoengineering. *npj Clim. Atmos. Sci.* **5**, 32 (2022).
- Xue, J. et al. Multidecadal variation of northern hemisphere summer monsoon forced by the SST inter-hemispheric dipole. *Environ. Res. Lett.* **17**, 44033 (2022).
- Zhou, C., Lu, J., Hu, Y. & Zelinka, M. D. Responses of the Hadley circulation to regional sea surface temperature changes. *J. Clim.* **33**, 429–441 (2020).

46. Rick, S. & Isaac, H. *General Circulation of the Atmosphere: 2000 Program of Study in Geophysical Fluid Dynamics*. 1–196 https://www.zhangqiaokeyan.com/ntis-science-report_ad_thesis/02071747702.html (2001).
47. Wang, N., Jiang, D. & Lang, X. Seasonality in the response of East Asian Westerly jet to the mid-Holocene forcing. *JGR Atmos.* **125**, e2020JD033003 (2020).
48. Liang, J. & Haywood, J. Future changes in atmospheric rivers over East Asia under stratospheric aerosol intervention. *Atmos. Chem. Phys.* **23**, 1687–1703 (2023).
49. Zhao, D. et al. Response of heterogeneous rainfall variability in East Asia to Hadley circulation reorganization during the late Quaternary. *Quat. Sci. Rev.* **247**, 106562 (2020).
50. Chiang, J. C. H. et al. Role of seasonal transitions and westerly jets in East Asian paleoclimate. *Quat. Sci. Rev.* **108**, 111–129 (2015).
51. Li, X., Lu, R. & Li, G. Different configurations of interannual variability of the western north pacific subtropical high and east asian westerly jet in summer. *Adv. Atmos. Sci.* **38**, 931–942 (2021).
52. Screen, J. A. et al. Consistency and discrepancy in the atmospheric response to Arctic sea-ice loss across climate models. *Nat. Geosci.* **11**, 155–163 (2018).
53. Woollings, T., Drouard, M., O'Reilly, C. H., Sexton, D. M. H. & McSweeney, C. Trends in the atmospheric jet streams are emerging in observations and could be linked to tropical warming. *Commun. Earth Environ.* **4**, 125 (2023).
54. Stendel, M., Francis, J., White, R., Williams, P. D. & Woollings, T. The jet stream and climate change. in *Climate Change*. 327–357 <https://doi.org/10.1016/B978-0-12-821575-3.00015-3> (Elsevier, 2021).
55. Barnes, E. A. & Screen, J. A. The impact of Arctic warming on the midlatitude jet-stream: can it? Has it? Will it? *WIREs Clim. Change* **6**, 277–286 (2015).
56. Sheng, C., Wu, G., Liu, Y. & He, B. Roles of thermal forced and eddy-driven effects in the northward shifting of the subtropical westerly jet under recent climate change. *J. Geophys. Res.* **129**, e2023JD039937 (2024).
57. Xing, C. & Liu, F. Mount Pinatubo eruption caused the major East China flood in 1991. *TIG* **1**, 100032 (2023).
58. Xie, S.-P. et al. Indo-western Pacific ocean capacitor and coherent climate anomalies in post-ENSO summer: a review. *Adv. Atmos. Sci.* **33**, 411–432 (2016).
59. Chen, L. et al. Drought in the Asian summer monsoon region is linked to a weakened inter-hemispheric temperature gradient. *Commun. Earth Environ.* **5**, 432 (2024).
60. Liu, J. et al. Dipolar mode of precipitation changes between north China and the Yangtze River Valley existed over the entire Holocene: evidence from the sediment record of Nanyi Lake. *Int. J. Climatol.* **41**, 1667–1681 (2021).
61. Seland, Ø et al. Overview of the Norwegian Earth System Model (NorESM2) and key climate response of CMIP6 DECK, historical, and scenario simulations. *Geosci. Model Dev.* **13**, 6165–6200 (2020).
62. Lawrence, D. M. et al. The community land model version 5: description of new features, benchmarking, and impact of forcing uncertainty. *J. Adv. Model Earth Syst.* **11**, 4245–4287 (2019).
63. Zhang, Y., MacMartin, D. G., Visioni, D., Bednarz, E. M. & Kravitz, B. Hemispherically symmetric strategies for stratospheric aerosol injection. *Earth Syst. Dynam.* **15**, 191–213 (2024).
64. Chen, W. et al. Recent progress in studies of the variabilities and mechanisms of the East Asian monsoon in a changing climate. *Adv. Atmos. Sci.* **36**, 887–901 (2019).
65. MacMartin, D. G. et al. The climate response to stratospheric aerosol geoengineering can be tailored using multiple injection locations. *J. Geophys. Res. Atmos.* **122**, 12,574–12,590 (2017).
66. Chen, C. C. et al. Climate impact of marine cloud brightening solar climate intervention under a susceptibility-based strategy simulated by CESM2. *J. Geophys. Res. Atmos.* **130**, e2024JD041245 (2025).
67. Asutosh, A., Tilmes, S., Bednarz, E. M. & Fadnavis, S. South Asian Summer Monsoon under stratospheric aerosol intervention. *npj Clim. Atmos. Sci.* **8**, 3 (2025).
68. Henry, M., Bednarz, E. M. & Haywood, J. How does the latitude of stratospheric aerosol injection affect the climate in UKESM1? *Atmos. Chem. Phys.* **24**, 13253–13268 (2024).
69. Richter, J. H. et al. Assessing responses and impacts of solar climate intervention on the earth system with stratospheric aerosol injection (ARISE-SAI): protocol and initial results from the first simulations. *Geosci. Model Dev.* **15**, 8221–8243 (2022).
70. Lauvset, S. K., Tjiputra, J. & Muri, H. Climate engineering and the ocean: effects on biogeochemistry and primary production. *Biogeosciences* **14**, 5675–5691 (2017).
71. Kristjánsson, J. E., Muri, H. & Schmidt, H. The hydrological cycle response to cirrus cloud thinning. *Geophys. Res. Lett.* **42**, 10,807–10,815 (2015).
72. Muri, H., Niemeier, U. & Kristjánsson, J. E. Tropical rainforest response to marine sky brightening climate engineering. *Geophys. Res. Lett.* **42**, 2951–2960 (2015).
73. Niemeier, U., Schmidt, H. & Timmreck, C. The dependency of geoengineered sulfate aerosol on the emission strategy. *Atmos. Sci. Lett.* **12**, 189–194 (2011).
74. Niemeier, U. & Timmreck, C. What is the limit of climate engineering by stratospheric injection of SO₂? *Atmos. Chem. Phys.* **15**, 9129–9141 (2015).
75. Hersbach, H. et al. The ERA5 global reanalysis. *Quart. J. R. Meteor. Soc.* **146**, 1999–2049 (2020).
76. Gou, J. et al. CNRD v1.0: a high-quality natural runoff dataset for hydrological and climate studies in China. *Bull. Am. Meteorol. Soc.* **102**, E929–E947 (2021).
77. Müller, R. C. et al. Radiative forcing geoengineering under high CO₂ levels leads to higher risk of Arctic wildfires and permafrost thaw than a targeted mitigation scenario. *Commun. Earth Environ.* **5**, 1–12 (2024).
78. Fan, Y. et al. Solar geoengineering can alleviate climate change pressures on crop yields. *Nat. Food* **2**, 373–381 (2021).
79. Park, C. et al. Inequal responses of drylands to radiative forcing geoengineering methods. *Geophys. Res. Lett.* **46**, 14011–14020 (2019).
80. Sun, P. et al. Nonstationarity-based evaluation of flood frequency and flood risk in the Huai River basin, China. *J. Hydrol.* **567**, 393–404 (2018).
81. Zhou, S., Yu, B., Lintner, B. R., Findell, K. L. & Zhang, Y. Projected increase in global runoff dominated by land surface changes. *Nat. Clim. Chang.* **13**, 442–449 (2023).
82. Zhou, S., Yu, B., Huang, Y. & Wang, G. The complementary relationship and generation of the Budyko functions. *Geophys. Res. Lett.* **42**, 1781–1790 (2015).
83. Yang, H. & Yang, D. Derivation of climate elasticity of runoff to assess the effects of climate change on annual runoff. *Water Resour. Res.* **47**, 2010WR009287 (2011).
84. Choudhury, B. Evaluation of an empirical equation for annual evaporation using field observations and results from a biophysical model. *J. Hydrol.* **216**, 99–110 (1999).
85. *Crop Evapotranspiration: Guidelines for Computing Crop Water Requirements*. (Food and Agriculture Organization of the United Nations, 1998).
86. Huang, Y., Wang, H., Fan, K. & Gao, Y. The Western Pacific Subtropical High after the 1970s: Westward or eastward shift? *Clim. Dyn.* **44**, 2035–2047 (2015).
87. Ling, S., Lu, R., Liu, H. & Yang, Y. Interannual meridional displacement of the upper-tropospheric westerly jet over Western East Asia in summer. *Adv. Atmos. Sci.* **40**, 1298–1308 (2023).
88. Huang, D.-Q., Zhu, J., Zhang, Y.-C. & Huang, A.-N. The different configurations of the East Asian polar front jet and subtropical jet and

- the associated rainfall anomalies over Eastern China in summer. *J. Clim.* **27**, 8205–8220 (2014).
89. Zhang, Y. & Huang, D. Has the East Asian westerly jet experienced a poleward displacement in recent decades? *Adv. Atmos. Sci.* **28**, 1259–1265 (2011).
 90. Richter, J. H. et al. Stratospheric dynamical response and ozone feedbacks in the presence of SO₂ injections. *J. Geophys. Res. Atmos.* **122**, 12,557–12,573 (2017).
 91. Zhou, W., Leung, L. R. & Lu, J. Seasonally and regionally dependent shifts of the atmospheric westerly jets under global warming. *J. Clim.* **35**, 5433–5447 (2022).
 92. Cui, X., Gao, Y. & Sun, J. The response of the East Asian summer monsoon to strong tropical volcanic eruptions. *Adv. Atmos. Sci.* **31**, 1245–1255 (2014).
 93. Dong, B., Sutton, R. T., Shaffrey, L. & Harvey, B. Recent decadal weakening of the summer Eurasian westerly jet attributable to anthropogenic aerosol emissions. *Nat. Commun.* **13**, 1148 (2022).
 94. Zhang, X. et al. Data and code for ‘Divergent impacts of climate interventions on China’s north-south water divide’. Zenodo <https://doi.org/10.5281/zenodo.16792015> (2025).
 95. Agency, J. M. Japanese reanalysis for three quarters of a century (JRA-3Q). UCAR/NCAR - Research Data Archive <https://doi.org/10.5065/AVTZ-1H78> (2023).
 96. European Space Agency. Copernicus Global Digital Elevation Model, distributed by OpenTopography. <https://doi.org/10.5069/G9028PQB> (2024).
 97. Xu, X. Spatial interpolation data set of mean state of meteorological elements in China. <https://doi.org/10.12078/2017121301> (2024).
 98. Liu, C. & Shi, R. GIS dataset of boundaries among four geo-eco regions of China. <https://doi.org/10.3974/geodb.2016.04.21.V1> (2016).
 99. Yuan, Q. et al. Spatio-temporal variation of the wet-dry conditions from 1961 to 2015 in China. *Sci. China Earth Sci.* **60**, 2041–2050 (2017).
 100. Yao, N., Li, Y., Lei, T. & Peng, L. Drought evolution, severity and trends in mainland China over 1961–2013. *Sci. Total Environ.* **616–617**, 73–89 (2018).
 101. Chen, J. et al. On the timing of the East Asian summer monsoon maximum during the Holocene—Does the speleothem oxygen isotope record reflect monsoon rainfall variability? *Sci. China Earth Sci.* **59**, 2328–2338 (2016).
 102. Nigam, S., Zhao, Y., Ruiz-Barradas, A. & Zhou, T. The south-flood north-drought pattern over eastern China and the drying of the Gangetic Plain. in *World Scientific Series on Asia-Pacific Weather and Climate* vol. 6, 347–359 (World Scientific, 2015).

Acknowledgements

This study was funded by the National Natural Science Foundation of China (42005130) and Shenzhen Science and Technology Program (No. ZDSYS20220606100806014). Y.F. acknowledges supports from the Scientific Research Start-up Funds (QD2023021C) from Tsinghua Shenzhen

International Graduate School. J.T. acknowledges supports from Research Council of Norway funded project NAVIGATE (352142). X.Z. acknowledges supports from the project of Key Laboratory of Changjiang Regulation and Protection of Ministry of Water Resources (QTKS0034W25089). Q.C. acknowledges supports from Chongqing Municipal Bureau of Water Resources (CQS23C01036, 5000002024CC20004) and Sichuan Province Regional Innovation Cooperation Project (2024YFHZ0098).

Author contributions

Y.F. designed the study and performed model simulations. X.Z. collected data and performed analyses. X.Z. and Y.F. drafted the manuscript. Y.F., X.Z., J.T., H.M., and Q.C. reviewed and edited the manuscript.

Competing interests

The authors declare no competing interests.

Additional information

Supplementary information The online version contains supplementary material available at <https://doi.org/10.1038/s43247-025-02708-0>.

Correspondence and requests for materials should be addressed to Yuanchao Fan.

Peer review information *Communications Earth & Environment* thanks the anonymous reviewers for their contribution to the peer review of this work. Primary handling editors: Sylvia Sullivan and Alireza Bahadori. A peer review file is available.

Reprints and permissions information is available at <http://www.nature.com/reprints>

Publisher’s note Springer Nature remains neutral with regard to jurisdictional claims in published maps and institutional affiliations.

Open Access This article is licensed under a Creative Commons Attribution 4.0 International License, which permits use, sharing, adaptation, distribution and reproduction in any medium or format, as long as you give appropriate credit to the original author(s) and the source, provide a link to the Creative Commons licence, and indicate if changes were made. The images or other third party material in this article are included in the article’s Creative Commons licence, unless indicated otherwise in a credit line to the material. If material is not included in the article’s Creative Commons licence and your intended use is not permitted by statutory regulation or exceeds the permitted use, you will need to obtain permission directly from the copyright holder. To view a copy of this licence, visit <http://creativecommons.org/licenses/by/4.0/>.

© The Author(s) 2025